

UC Berkeley

UC Berkeley Previously Published Works

Title

Optimizing the monomer structure of polyhedral oligomeric silsesquioxane for ion transport in hybrid organic-inorganic block copolymers

Permalink

<https://escholarship.org/uc/item/141576d4>

Journal

Journal of Polymer Science, 58(2)

ISSN

2642-4150

Authors

Gao, Kevin W
Jiang, Xi
Hoffman, Zach J
[et al.](#)

Publication Date

2020-01-15

DOI

10.1002/pol.20190073

Peer reviewed

**1 Optimizing the Monomer Structure of Polyhedral
2 Oligomeric Silsesquioxane (POSS) for Ion Transport in
3 Hybrid Organic-Inorganic Block Copolymers**

**4 Kevin W. Gao,^{a,b,d} Xi Jiang,^b Zach J. Hoffman,^{a,b,d} Gurmukh K. Sethi,^{b,c}
5 Saheli Chakraborty,^{a,b} Irune Villaluenga,^{a,*} Nitash P. Balsara^{a,b,d,*}**

*6^a Department of Chemical and Biomolecular Engineering, University of
7 California, Berkeley, California 94720, USA*

*8^b Materials Sciences Division, Lawrence Berkeley National Laboratory,
9 Berkeley, California 94720, USA*

*10^c Department of Materials Science and Engineering, University of California,
11 Berkeley, California 94720, USA*

*12^d Joint Center for Energy Storage Research (JCESR), Lawrence Berkeley
13 National Laboratory, Berkeley, California 94720, USA*

14* Correspondence to nbalsara@berkeley.edu and irvillaleunga@gmail.com

ABSTRACT

Poly(ethylene oxide)-*b*-polyhedral oligomeric silsesquioxane (PEO-POSS) mixed with lithium bis(trifluoromethanesulfonyl)imide salt is a nanostructured hybrid organic-inorganic block copolymer electrolyte that may enable lithium metal batteries. The synthesis and characteristics of three PEO-POSS block copolymer electrolytes which only differ by their POSS silica cage substituents (ethyl, isobutyl, isooctyl) is reported. Changing the POSS monomer structure results in differences in both thermodynamics and ion transport. All three neat polymers exhibit lamellar morphologies. Adding salt results in the formation of a disordered window which closes and gives way to lamellae at higher salt concentrations. The width of disordered window decreases with increasing length of the POSS alkyl chain substituent from ethyl to isobutyl and is absent in the isooctyl sample. Rheological measurements demonstrate good mechanical rigidity when compared with similar all-organic block copolymers. While salt diffusion coefficient and current ratio are unaffected by substituent length, ionic conductivity increases as the length of the alkyl chain substituent decreases: the ethyl substituent is optimal for ion transport. This is surprising because conventional wisdom suggests that ion transport occurs primarily in the PEO-rich domains, i.e. ion transport should be unaffected by substituent length after accounting

15

16 INTRODUCTION

17 Solid polymer electrolytes
18 are of interest for developing safer
19 lithium batteries as they are less
20 flammable than more traditional
21 organic liquid electrolytes.¹⁻³ They
22 may also enable the development
23 of higher energy density batteries
24 with lithium metal anodes.⁴⁻⁵ In
25 order to be used in lithium metal
26 batteries, polymer electrolytes
27 must have good ion transport
28 properties as well as high
29 mechanical rigidity to prevent
30 lithium dendrite growth.⁶ These two
31 properties are decoupled in block
32 copolymers such as polystyrene-*b*-
33 poly(ethylene oxide) (SEO) wherein
34 the polystyrene-rich microphase

35 provides mechanical strength and
36 the poly(ethylene oxide)-rich
37 microphase enables ion transport
38 when a salt such as lithium
39 bis(trifluoromethanesulfonyl)imide
40 (LiTFSI) is mixed with the
41 copolymer.⁷ The phase behavior of
42 these materials is also important,
43 as ion transport parameters such
44 as ionic conductivity and salt
45 diffusion coefficient are affected by
46 morphology.⁸ Most of the work in
47 this area is restricted to all-organic
48 block copolymer systems.⁸⁻²²

49 Recent work has shown that
50 hybrid organic-inorganic
51 poly(ethylene oxide)-*b*-polyhedral
52 oligomeric silsesquioxane (PEO-
53 POSS) block copolymers with LiTFSI

51self-assemble into a variety of
52morphologies with high mechanical
53rigidity and ionic conductivity when
54compared with SEO electrolytes of
55comparable molecular weight.²³
56Like in SEO, the PEO-rich
57microphase facilitates ion transport
58via segmental motion,²⁴ while the
59POSS-rich microphase furnishes
60mechanical rigidity.²⁵ While it is
61clear that the thermodynamic
62interactions between PEO and
63POSS chains depend on the
64chemical structure of the silica
65cage substituents on the POSS
66monomer, effect of the cage
67structure on ion transport is an
68open question. While the impact of
69cage substituents on the thermal
70and morphological characteristics
71of nanocomposite polymer - POSS
72blends has often been studied,²⁶⁻³⁵
73sparse work on its effect upon
74phase behavior and ion transport in
75block copolymers exists.³⁶⁻³⁸

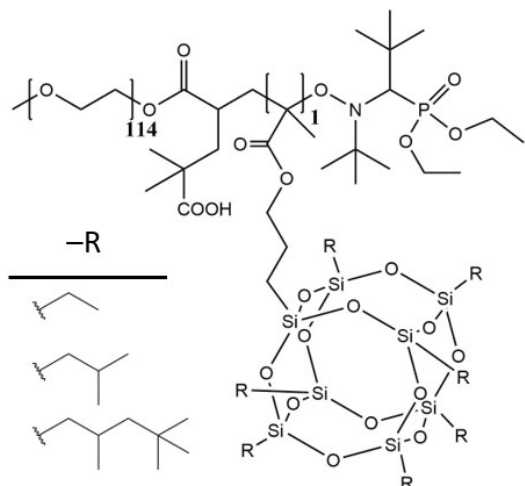
76 In this paper, we report on
77the synthesis of PEO-POSS block
78copolymers from three different
79POSS containing monomers
80(methacrylethyl, methacrylisobutyl,
81methacrylisooctyl POSS) whose
82cage substituents systematically
83increase in alkyl chain length. We
84use small angle X-ray scattering
85(SAXS) and transmission electron
86microscopy (TEM) to determine the
87morphology of these systems with
88and without added salt. The
89mechanical properties of the neat
90polymers are determined through
91rheological measurements. Finally,
92electrochemical characterization is
93used to study ion transport.

94 Conventional wisdom
95suggests that the chemical
96composition of the non-conducting
97microphase does not affect ion
98transport of block copolymer
99electrolytes, after effects related to
100changes in the morphology and
101volume fraction of the conducting
102phase are accounted for.^{8,14,19,39-40}
103The purpose of this paper is to
104challenge this conventional
105wisdom.

106EXPERIMENTAL

107 The PEO-POSS copolymers
108were synthesized, purified, and
109characterized using methods
110described in **ref 23** and reported in
111the Supporting Information
112(**Figures S1-S7**). The polymers
113used in this study are called PEO-
114POSS(5-1) where the 5 denotes the
115molecular weight of PEO in kg mol⁻¹
116and there is 1 POSS unit of varying
117molecular weight from 0.7 to 1.3 kg
118mol⁻¹ due to the different alkyl
119chain substituent (ethyl, isobutyl,
120isooctyl) on the POSS silica cage.
121The chemical structure is shown in
122**Figure 1**.

123 We add LiTFSI salt to make
124electrolytes of varying salt
125concentration r , where we define r
126to be the molar ratio of lithium to
127ethylene oxide moieties.
128Electrolytes were prepared with
129methods described in **ref 23**. A list
130of the polymer characteristics can
131be found in **Table 1**. The neat
132copolymers are colorless.



133
 134 **Figure 1.** Chemical structure of PEO-
 135 POSS polymers synthesized. The alkyl
 136 substituent on the POSS silica cage
 137 increases in length from ethyl to
 138 isobutyl to isooctyl.

139 **Table 1.** Summary of PEO-POSS(5-1)
 140 characteristics

| -R | M_{POSS} (kg/m ³) | M_{PEO} (kg/m ³) | $f_{\text{EO/LITFSI}}$ | N |
|----------|---|--|------------------------|-----|
| Ethyl | 0.7 | 5 | 0.87 - 0.93 | 85 |
| Isobutyl | 0.9 | 5 | 0.85 - 0.92 | 87 |
| Isooctyl | 1.3 | 5 | 0.79 - 0.88 | 95 |

142 Small angle X-ray scattering 143 (SAXS)

144 SAXS samples were prepared
 145 by melt pressing the polymer into a
 146 0.766 cm thick rubber spacers with
 147 a 0.3175 cm inner diameter, and
 148 annealing them at 90 °C for 3
 149 hours, then 70 °C for 48 hours
 150 before allowing them to cool slowly
 151 under vacuum to room

152 temperature. The samples were
 153 sealed with Kapton windows in
 154 custom-designed airtight aluminum
 155 holders.

156 SAXS measurements were
 157 performed at beamline 1-5 at the
 158 Stanford Synchrotron Radiation
 159 Lightsource and SLAC National
 160 Accelerator Laboratory and
 161 beamline 7.3.3 at the Advanced
 162 Light Source at Lawrence Berkeley
 163 National Laboratory.⁴¹ Silver
 164 behenate was used to determine
 165 the beam center and sample-to-
 166 detector distance. The scattered
 167 intensity was corrected for beam
 168 transmission and empty cell
 169 scattering. Two dimensional
 170 scattering patterns were integrated
 171 azimuthally using the Nika program
 172 for IGOR Pro to produce one-
 173 dimensional scattering profiles and
 174 are reported as scattering
 175 intensity, I , as a function of the
 176 magnitude of the scattering vector,
 177 q .⁴² Absolute scattering intensity,
 178 I_{abs} , was obtained by calibrating to
 179 a glassy carbon absolute intensity
 180 standard and is reported in the
 181 Supporting Information (**Figure**
 182 **S12**). Measurements were taken in
 183 a custom-built 8-sample heating
 184 stage at 70 °C, 90 °C, and 110 °C.
 185 Samples were equilibrated for
 186 about 20 min at each temperature
 187 before taking measurements. To a
 188 good approximation, the SAXS
 189 profiles of all our samples were
 190 independent of temperature in the
 191 temperature range of 70 - 110 °C
 192 and were similar upon heating and
 193 cooling. We only discuss data
 194 obtained at 70 °C in the main text
 195 in consistency with our
 196 electrochemical measurements.

158The temperature range of our SAXS
159experiments is above the melting
160temperature of the semi-crystalline
161PEO block.

162**Electrochemical measurements**

163 All sample preparation was
164performed inside of an argon
165glovebox with water and oxygen
166levels below 1 ppm and 2 ppm
167respectively. Conductivity cells
168were prepared by pressing the
169polymer electrolyte into a 254 μm
170thick silicone spacer with a 1/8 in.
171inner diameter and sandwiching
172between two 200 μm thick
173stainless-steel shim blocking
174electrodes. Lithium symmetric cells
175were prepared by pressing the
176polymer electrolyte into a 254 μm
177thick silicone spacer with a 1/8 in.
178inner diameter and sandwiching
179between two 180 μm thick lithium
180foils backed with stainless-steel
181shims. For both conductivity and
182lithium symmetric cells, nickel tabs
183were secured to the stainless-steel
184shims to serve as electrical
185contacts, and the assembly was
186vacuum sealed in laminated
187aluminum pouch material. Each cell
188was then taken out of the
189glovebox, placed in a custom-built
190heating stage, and annealed at 90
191 $^{\circ}\text{C}$ for 3 hours prior to
192electrochemical characterization.
193At the conclusion of the
194experiments, samples were taken
195back into the glovebox to check for
196defects and the assembly was
197measured to find the final sample
198thickness.

199 Complex impedance
200measurements were performed on
201the conductivity cells via a Bio-

202Logic VMP3 potentiostat over a 0.1
203- 10^6 Hz frequency range at an
204amplitude of 80 mV to find the
205ionic conductivity, κ .
206Representative Nyquist plots are
207shown in the Supporting
208Information (**Figure S13**). Lithium
209symmetric cells were first
210conditioned for at least 4
211charge/discharge cycles at a low
212current density of 0.02 mA cm^{-2} to
213ensure a stable interfacial layer
214was introduced. Each conditioning
215cycle consisted of a 4 h charge
216followed by a 2 h rest and a 4 h
217discharge. The Bruce and Vincent
218method was then used to find the
219current fraction, ρ_+ , defined as

$$220 \rho_{+i} = \frac{i_{ss}(\Delta V - i_{\Omega} R_{i,0})}{i_{\Omega} \Delta V}$$

221where $R_{i,0}$ is the initial interfacial
222resistance, $R_{i,ss}$ is the interfacial
223resistance at steady-state, i_{ss} is the
224current measured at steady state,
225 ΔV is the applied potential, i_{Ω} is a
226measure of the initial current, as
227defined by the ratio of the applied
228potential to the sum of the initial
229bulk and interfacial resistances.⁴³
230The restricted diffusion method
231was used to find the salt diffusion
232coefficient, D .⁴⁴ Cells were polarized
233at +/- 10 mV and +/- 20 mV until a
234steady-state current was reached,
235then allowed to relax under open
236circuit potentials. Impedance was
237taken before and after polarization.
238Measurements were done at 70 $^{\circ}\text{C}$.

239 In the literature, the
240parameter we call ρ_+ is often
241referred to as the transference
242number.⁴⁵ In our group, we have
243referred to it as the steady state
244cationic transference number, $t_{+,ss}$.

245 It has been shown that ρ_+ (or $t_{+,ss}$)
246 is equal to the transference
247 number in dilute and ideal
248 electrolytes.⁴⁶ However, in
249 concentrated electrolytes, and
250 especially in concentrated polymer
251 electrolytes, there is a significant
252 difference in both magnitude and
253 sign between ρ_+ and the
254 transference number.⁴⁵⁻⁴⁷ Since we
255 are mainly interested in
256 concentrated electrolytes in this
257 work and it has been shown that
258 PEO-containing electrolytes are
259 highly non-ideal⁴⁷, we use the term
260 ρ_+ to indicate the results of these
261 experiments using the Bruce and
262 Vincent method.

263 Rheology

264 The viscoelastic properties of
265 the neat polymers were studied
266 using the procedure outlined in **ref**
267 **48**, though samples were prepared
268 by annealing at 70 °C instead of
269 120 °C. Measurements were
270 repeated multiple times.-

271 Transmission electron 272 microscopy imaging

273 The quenched PEO-POSS bulk
274 samples were sectioned at -120 °C
275 using a cryo-microtome (Leica
276 Ultracut 6) to obtain ultrathin
277 films (~100 nm). The ultrathin films
278 were transferred to copper grids
279 with lacey carbon supporting film
280 and stored in an argon glovebox
281 immediately after cryo-
282 microtoming to minimize the effect
283 of humidity. PEO-rich domains were
284 stained to increase contrast and
285 stability under the electron beam
286 by exposing the ultrathin film to
287 ruthenium tetroxide vapor for 10

288 minutes at room temperature. TEM
289 micrographs were collected using
290 Philips CM200 equipped with Gatan
291 US1000 CCD camera.

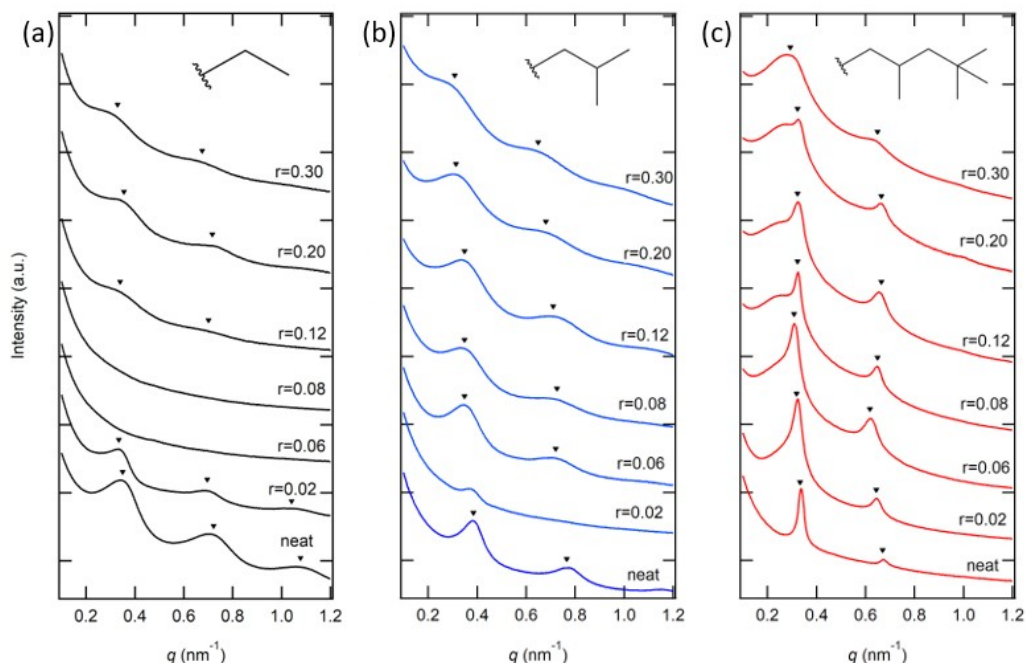
292 RESULTS AND DISCUSSION

293 We performed SAXS
294 experiments to elucidate the
295 morphology of our electrolytes.
296 Typical data obtained are shown in
297 Figure 2 where scattering intensity
298 measured at 70 °C is plotted as a
299 function of the magnitude of the
300 scattering vector. In **Figure 2a**, we
301 show data obtained from ethyl
302 samples with varying salt
303 concentration. In the neat state,
304 the ethyl polymer exhibits a
305 lamellar morphology, as evidenced
306 by the scattering peaks at $q = q^*$,
307 $2q^*$, and $3q^*$ where q^* indicates
308 the location of the primary
309 scattering peak. Upon salt addition,
310 at $r = 0.02$, the peaks diminish in
311 intensity, and at $r = 0.06$ the peaks
312 vanish, indicating the formation of
313 a disordered phase. Upon further
314 increase in salt concentration to r
315 = 0.12, weak scattering peaks
316 corresponding to a lamellar phase
317 appear and their intensity
318 increases with increasing salt
319 concentration. In **Figure 2b**, we
320 show data obtained from isobutyl
321 samples with varying salt
322 concentration. This polymer also
323 forms a lamellar phase in the neat
324 state. Increasing r to 0.02 results in
325 a loss of the peak at $q = 2q^*$ and a
326 significant reduction in scattering
327 intensity at $q = q^*$. We attribute
328 this weak scattering peak to the
329 presence of disordered
330 concentration fluctuations.⁴⁹ The
331 isooctyl sample is lamellar in the

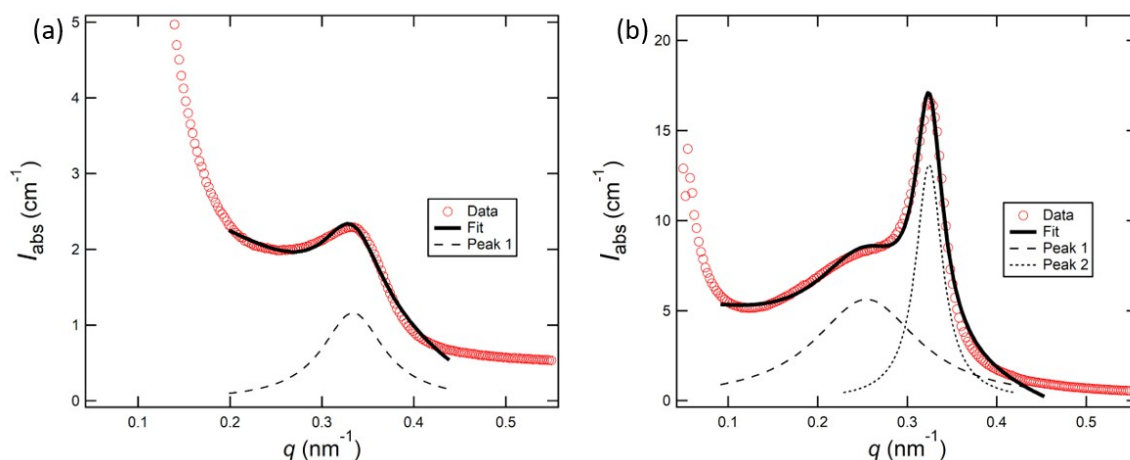
295 neat state with relatively sharp
296 peaks at q^* and $2q^*$, as can be
297 seen in **Figure 2c**. The addition of
298 salt results in an increase in the
299 scattering intensity at q values
300 below q^* (in the range $0.20 \text{ nm}^{-1} \leq$
301 $q \leq 0.35 \text{ nm}^{-1}$). At $r = 0.08$, a
302 distinct shoulder is apparent in this
303 q range. This shoulder becomes
304 more pronounced with increasing
305 salt concentration. At $r = 0.3$, we
306 obtain broad scattering peaks that
307 are reminiscent of the scattering
308 peaks seen in the ordered ethyl
309 and isobutyl samples.

310 To better quantify the
311 ordering in our systems, we
312 analyze the absolute scattering
313 intensities of each sample. These
314 profiles, qualitatively similar to the
315 raw scattering profiles of **Figure 2**,
316 are given in **Figure S12** in the
317 Supporting Information. In **Figure**
318 **3a**, we show scattering in the
319 vicinity of the primary peak for the

320 ethyl sample at $r = 0.02$. A
321 Lorentzian fit (with a linear
322 background) through the data is
323 shown by the curve. The primary
324 peak after background subtraction
325 is shown as a dashed curve in
326 **Figure 3a**. This enables
327 determination of the full-width-half-
328 max (FWHM), which for the sample
329 in **Figure 3a** is 0.082 nm^{-1} . In
330 **Figure 3b**, we show scattering in
331 the vicinity of the primary peak for
332 the isooctyl sample at $r = 0.12$.
333 Clearly, a single Lorentzian is not
334 consistent with this data set, and
335 we thus use a two Lorentzian fit to
336 characterize this sample. This
337 enables determination of two
338 FWHM values corresponding to the
339 two peaks shown in **Figure 3b**
340 (0.14 and 0.036 nm^{-1}). All of the
341 scattering curves from the ethyl
342 and isobutyl samples were
343 analyzed using the approach



344 **Figure 2.** Scattering intensity at 70 °C of the three PEO-POSS polymers with
 345 various salt concentrations, plotted as a function of the magnitude of the scattering
 346 vector, q , (a) ethyl (b) isobutyl and (c) isoctyl. Profiles are shifted vertically.
 347 Triangles indicate peaks at q^* , $2q^*$, and $3q^*$ (when identified). These peaks signify
 348 lamellar order.



349 **Figure 3.** Lorentzian fits of the scattering around the primary peak for the (a) $r =$
 350 0.02 ethyl sample, with a FWHM of 0.082 nm⁻¹, and the (b) $r = 0.12$ isoctyl sample,
 351 which has FWHMs of 0.14 and 0.036 nm⁻¹.

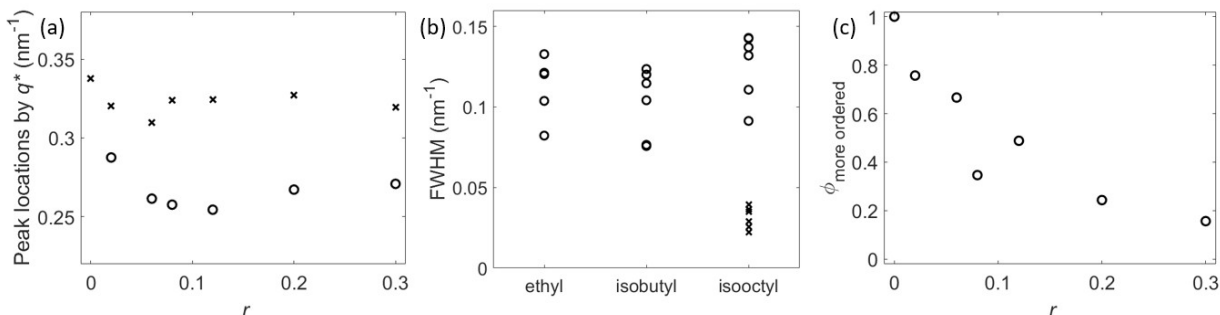
352 shown in **Figure 3a**. The scattering
 353 curve from the neat isoctyl
 354 sample was analyzed using one
 355 Lorentzian while the salty samples

356 were analyzed using two
 357 Lorentzians as in **Figure 3b**.

358 In **Figure 4a** we compare
 359 the locations of the scattering

360 peaks in the salty isooctyl samples.
 361 There is a clear distinction between
 362 the broad and sharp peaks. In
 363 **Figure 4b**, we plot the FWHMs

364 obtained from our fitting procedure
 365 outlined above. The widths of the
 366 primary scattering peaks



367 **Figure 4.** (a) Plot of the peak locations around q^* in the isooctyl samples versus
 368 salt concentration, where the circles denote the broad peaks and the x's denote the
 369 sharp peaks. (b) Plot of the full-width-half-max of the primary scattering peak
 370 versus POSS silica cage alkyl substituent, where circles denote the broad peaks
 371 found in the ethyl, isobutyl and salty isooctyl samples, and x's denote the sharp
 372 peaks in the isooctyl samples. (c) Plot of the volume fraction of the phase in the
 373 isooctyl electrolytes with more long range order versus salt concentration, r .

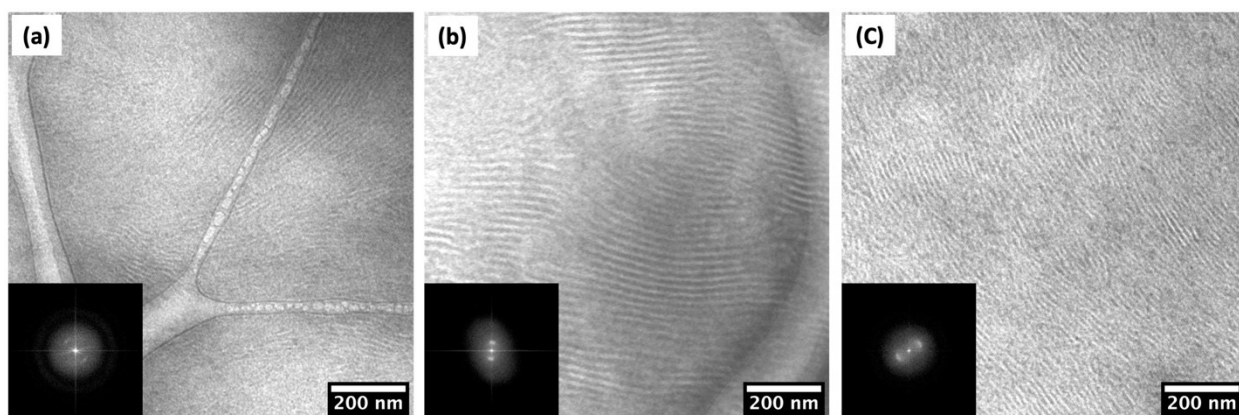
374 of the ethyl and isobutyl samples
 375 are similar, and we obtain FWHMs
 376 between 0.07 and 0.13 nm^{-1} . We
 377 obtain two sets of FWHM values for
 378 the isooctyl samples, one set that
 379 is qualitatively similar to that of the
 380 ethyl and isobutyl samples, and
 381 another with significantly lower
 382 FWHM values ranging from 0.02 to
 383 0.04 nm^{-1} . It is perhaps interesting
 384 to note that the FWHM of the
 385 ordered phase formed in the neat
 386 isooctyl sample is qualitatively
 387 different than those obtained in the
 388 other samples, both with and
 389 without salt. The addition of salt to
 390 the isooctyl sample results in the
 391 emergence of a broad scattering
 392 profile that is qualitatively similar
 393 to that obtained from the other
 394 samples. The FWHM is generally
 395 assumed to be an indication of the
 396 extent of long range order. We
 397 conclude that the salt-containing

398 isooctyl samples comprise two
 399 kinds of ordered phases with
 400 distinct extents of long range
 401 order. In **Figure 4c** we compare
 402 the volume fractions of the two
 403 coexisting phases in our salty
 404 isooctyl samples by integrating
 405 $I_{\text{abs}} q^2$ of the broad and sharp peaks
 406 (see **Figure 3b**) using a procedure
 407 outlined in **ref 50**. The volume
 408 fraction of the phase with greater
 409 long range order decreases with
 410 increasing salt concentration.

411 Samples were annealed at 70
 412 $^{\circ}\text{C}$ and quenched in liquid nitrogen
 413 to “freeze” the morphology at
 414 these temperatures before
 415 performing electron microscopy.
 416 The resulting TEM micrographs are
 417 shown in **Figure 5**, where the dark
 418 phase represents the RuO_4 stained
 419 PEO-rich microphases. The
 420 micrographs obtained from those

421 samples show similar alternating
 422 dark and bright stripes, PEO-rich
 423 and POSS-rich domains,
 424 representing the lamellar phase
 425 separation. **Figure 5a** shows the
 426 typical lamellar morphology in the
 427 neat ethyl sample. As shown in
 428 **Figure 5b**, the lamellar structure
 429 in the isooctyl sample exhibits a
 430 more long-range ordered structure
 431 with larger spacing (d). In addition,
 432 the Fourier transforms of the
 433 micrographs suggest that the
 434 isooctyl sample has the largest d
 435 as compared to the d in neat ethyl

436 sample and the salty isooctyl
 437 sample ($r = 0.12$). The distinction
 438 between the two kinds of lamellar
 439 phases in salty isooctyl samples is
 440 not evident by the micrograph in
 441 **Figure 5c**. We note that similar
 442 data (i.e. the presence of an
 443 additional peak in the vicinity of
 444 the primary peak) have been
 445 obtained from other salty block
 446 copolymers. The presence of
 447 coexisting phases is clearly seen by
 448 TEM in some cases²²⁻²³, but not in
 449 others⁵¹. In **ref 51**, the presence of
 450 an

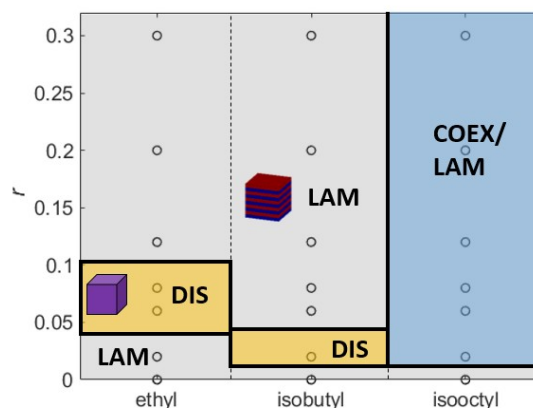


451 **Figure 5.** TEM micrographs of (a) neat ethyl sample, (b) neat isooctyl sample, and
 452 (c) isooctyl $r = 0.12$. The dark phase represents the RuO_4 stained PEO domain.
 453 Insets show the Fourier transforms of the micrographs. Lamellar order is seen in all
 454 cases.

455 additional peak was attributed to
 456 the formation of a superlattice.
 457 Further work is needed to establish
 458 the origin of the SAXS pattern
 459 shown in **Figure 4b**.

460 The effect of added salt and
 461 monomer structure on morphology
 462 is summarized in **Figure 6**. In ethyl
 463 and isobutyl samples, we only see
 464 lamellae and disorder. In the
 465 isooctyl samples, we see lamellae
 466 in the neat state and coexisting
 467 phases in the presence of added
 468 salt. The thermodynamic

469 interactions between the PEO and
 470 POSS blocks in the presence of salt
 471 is complex. Disordered phases are
 472 formed upon salt addition but this
 473 applies to a limited window of salt
 474 concentrations. When this window
 475 is exceeded, ordered phases

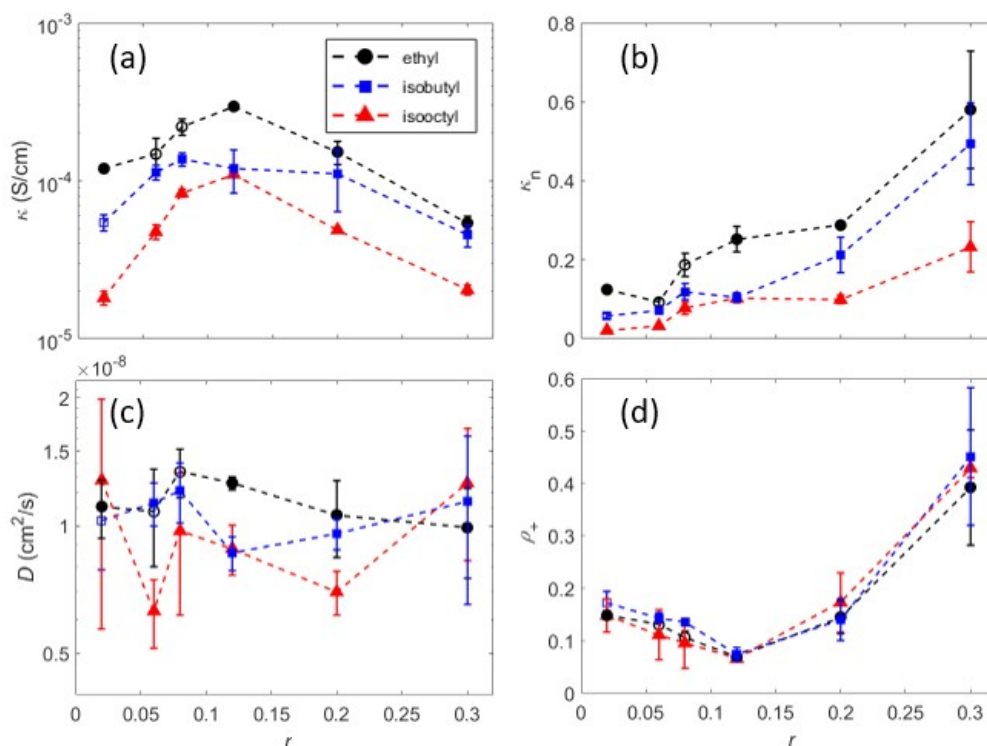


476reappear at high salt
 477concentrations. The salt
 478concentration window for which
 479disordering occurs decreases as we
 480increase the POSS alkyl substituent
 481chain length and is absent in the
 482isooctyl sample. There are many
 483possible reasons for the complex
 484phase behavior seen in **Figure 6**.
 485This includes differences in polarity
 486of the POSS block, shielding of
 487repulsive interactions between the
 488POSS particle and PEO due to the
 489presence of alkyl substituents, and
 490the distribution of ions in PEO-rich
 491and POSS-rich domains. Partial
 492solubility of LiTFSI in the POSS-rich
 493domains may account for
 494differences in phase behavior. It is
 495evident that segregation and phase

496separation in PEO-POSS(5-1) block
 497copolymers is greatly affected by
 498the functional groups on the POSS
 499monomer.

500**Figure 6.** Morphology of phases on a
 501salt concentration, r , versus POSS
 502silica cage alkyl substituent plot:
 503lamellar (LAM) and disordered (DIS),
 504as well as a coexistence of ordered
 505phases (COEX/LAM).

506 We measured the ionic
 507conductivity, salt diffusion
 508coefficient, and the current ratio of
 509the three PEO-POSS(5-1) systems
 510in order to determine the effect of
 511POSS alkyl substituent length on
 512ion transport. In **Figure 7a** we see
 513that upon salt addition, the
 514conductivity for all three PEO-
 515POSS(5-1)



516**Figure 7.** (a) Ionic conductivity from ac impedance spectroscopy of symmetric cells
 517with blocking electrodes. (b) Normalized conductivity, κ_n , using PEO (10 kg mol^{-1})
 518data. For all salt concentrations, the normalized conductivity decreases as we
 519increase the alkyl substituent length. (c) Salt diffusion coefficient from restricted

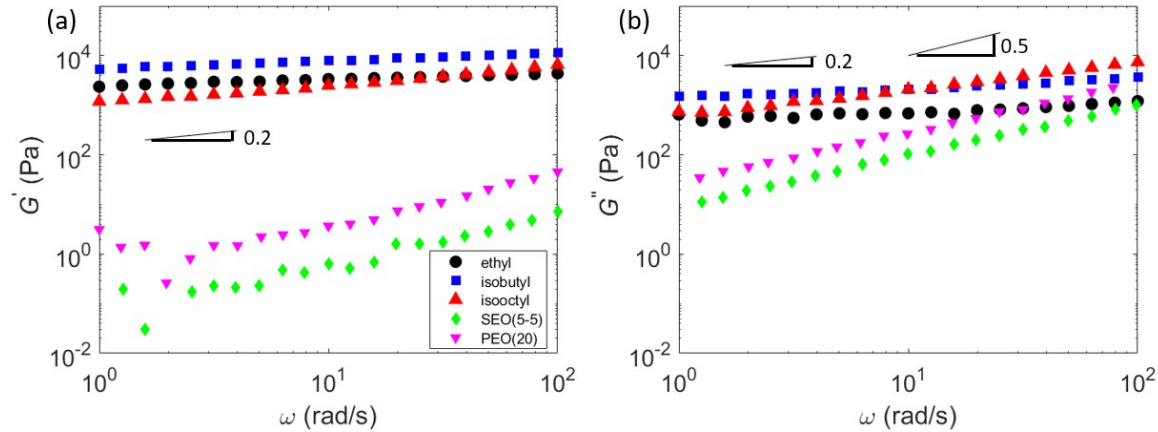
520 diffusion measurements in a lithium symmetric cell. (d) Current fractions calculated
521 from the Bruce-Vincent method using a lithium symmetric cell. Data was taken at
522 70 °C. The solid markers denote ordered morphologies while open face markers
523 correspond to a disordered phase.

524 polymers increase until they reach
525 a maximum at around $r = 0.12$
526 before decreasing at higher salt
527 concentrations. Ionic conductivity
528 in polymer electrolytes depends on
529 both charge concentration and
530 segmental motion.²⁴ The glass
531 transition temperature is a simple
532 measure of this segmental
533 relaxation. In our system, the glass
534 transition temperature increases as
535 salt is added (see **Figures S8-**
536 **S10**) due to ion and polymer
537 associations, from -45 °C at $r =$
538 0.08 to -15 °C at $r = 0.30$ (all of the
539 PEO-POSS(5-1) samples exhibit
540 similar behavior; see **Figure S11**).
541 The peak in the conductivity curves
542 in **Figure 7a** arises due to the
543 interplay between the increase in
544 charge carrier concentration and
545 the slowing down of segmental
546 relaxation.

547 We can account for the
548 volume fraction of the conducting
549 phase, ϕ_c , to get a better idea of
550 the differences in intrinsic
551 conductivities across the three
552 systems by utilizing the following
553 equation: $\kappa_n = \kappa_{PEOPOSS} \phi_c^{-1} \kappa_{PEO}^{-1}$,
554 where κ_{PEO} is the ionic conductivity
555 of PEO (10 kg mol⁻¹) at 70 °C.
556 Previous studies suggest that the
557 ionic conductivity of PEO/LiTFSI
558 mixtures is independent of
559 molecular weight when it exceeds
560 2 kg mol⁻¹.⁵² Increasing the length
561 of the alkyl substituents reduces ϕ_c
562 at fixed chain length. The plot of
563 normalized conductivity, κ_n , versus
564 POSS silica cage alkyl substituent is

565 shown in **Figure 7b**. Even after
566 accounting for differences in ϕ_c
567 (see **Figure S14**), the ethyl
568 samples show the highest
569 conductivity, especially in the
570 vicinity of the conductivity
571 maximum. It is perhaps surprising
572 that the greatest normalized
573 conductivity is at the highest salt
574 concentration, $r = 0.30$. We posit
575 that at high salt concentration,
576 some of the LiTFSI molecules are
577 located in the POSS-rich
578 microphase due to entropic
579 reasons. This will result in a lower
580 salt concentration in the
581 conducting PEO-rich domains,
582 which, in turn, will increase the
583 intrinsic conductivity of these
584 domains as the conductivity of PEO
585 decreases with increasing salt
586 concentration for $r > 0.10$.⁴⁷ The
587 concentration dependence of the
588 salt diffusion coefficient is shown in
589 **Figure 7c**. Neither salt
590 concentration nor alkyl chain
591 length has a strong influence on
592 this parameter, which falls around
593 10^{-8} cm² s⁻¹ for all three PEO-
594 POSS(5-1) systems. The
595 concentration dependence of the
596 current fraction shown in **Figure**
597 **7d** is similar to that reported for
598 SEO/LiTFSI mixtures and is
599 independent of alkyl chain length.⁴⁷

600 We compare the mechanical
 601 properties of neat PEO-POSS(5-1)
 602 to neat PEO(20) with a molecular
 603 weight of 20 kg mol⁻¹ and neat



604 SEO(5-5) which has two blocks of
 605 molecular weight 5 kg mol⁻¹. (We
 606 choose SEO(5-5) because it
 607 exhibits lamellar order.) The
 608 storage modulus, G' , of the PEO-
 609 POSS(5-1) polymers, shown in
 610 **Figure 8a**, is a weak function of
 611 frequency, typical of solid-like
 612 polymers. The magnitude of G' of
 613 all three of our PEO-POSS(5-1)
 614 polymers is similar. In the low
 615 frequency limit, $G' \sim \omega^{0.2}$ for all
 616 three PEO-POSS(5-1) polymers.
 617 Amongst the polymers covered in
 618 this study, the isobutyl sample
 619 exhibits the highest storage
 620 modulus. G' of PEO-POSS(5-1)
 621 polymers is higher than that of
 622 PEO(20) and SEO(5-5) by factors
 623 between 10^2 and 10^3 . The
 624 frequency dependence of the loss
 625 modulus, G'' , is shown in **Figure**
 626 **8b**. G'' is a weak function of
 627 frequency for PEO-POSS(5-1)
 628 polymers. In the low frequency
 629 limit, $G'' \sim \omega^{0.2}$ for the ethyl and
 630 isobutyl samples. For the isooctyl
 631 sample $G'' \sim \omega^{0.5}$. At high
 632 frequencies, G'' of these polymers

602 is comparable to that of PEO(20)
603 and SEO(5-5). At low frequencies,
604 G'' of PEO-POSS(5-1) polymers is
605 about a factor of 10 higher than

606 SEO(5-5). Both G' and G'' of
607 PEO(20) and SEO(5-5) decrease
608 rapidly with decreasing frequency.

609 **Figure 8.** (a) Storage and (b) loss moduli as a function of frequency for PEO-
610 POSS(5-1), SEO(5-5), and PEO(20). All three PEO-POSS(5-1) polymers exhibit greater
611 mechanical rigidity than SEO(5-5) and PEO(20).-

612 CONCLUSIONS

613 We have synthesized and
614 characterized a set of three PEO-
615 POSS(5-1) block copolymer
616 electrolytes with ethyl, isobutyl,
617 and isooctyl substituents on the
618 POSS silica cage. These
619 electrolytes primarily exhibit
620 lamellar morphologies. If only
621 interactions between the salt and
622 PEO were important, then changing
623 the monomer structure of the non-
624 conducting block would have a
625 minimal effect on both
626 thermodynamics and transport. We
627 show, however, that this is not the
628 case. Increasing the length of the
629 POSS alkyl chain substituent leads
630 to a smaller salt concentration
631 window for disorder. In the isooctyl
632 case, no disordered window is
633 observed. Instead, we find
634 coexisting ordered phases that are
635 absent in the ethyl and isobutyl
636 samples. The ethyl samples exhibit
637 the highest ionic conductivity even
638 after normalizing for the volume
639 fraction of conducting phase. The
640 salt diffusion coefficient and
641 current ratio are not affected by
642 the alkyl substituent length. These
643 results indicate that the ethyl
644 systems are optimal for ion
645 transport applications. Further
646 investigation is needed to better
647 understand the relationship
648 between the thermodynamic

649 behavior and ion transport in these
650 hybrid organic-inorganic systems.

651

652 ACKNOWLEDGEMENTS

653 This work was intellectually
654 led by the Joint Center for Energy
655 Storage Research (JCESR), an
656 Energy Innovation Hub funded by
657 the U.S. Department of Energy,
658 Office of Science, Office of Basic
659 Energy Science, under Contract No.
660 **DE-AC02-06CH11357**, which
661 supported both synthesis and
662 characterization work conducted by
663 K.W.G. under the supervision of
664 N.P.B. Work at the Donner Lab, the
665 Molecular Foundry, and the
666 Advanced Light Source, which is a
667 DOE Office of Science User Facility,
668 was supported by Contract No. **DE-**
669 **AC02-05CH11231**. Work at the
670 Stanford Synchrotron Radiation
671 Light Source, a user facility at SLAC
672 National Accelerator Laboratory,
673 was supported by the U.S.
674 Department of Energy, Office of
675 Science, Office of Basic Energy
676 Science under Contract No. **DE-**
677 **AC02-76SF00515**. K.W.G.
678 acknowledges funding from a
679 National Defense and Science
680 Engineering Graduate Fellowship.
681

682 CONFLICTS OF INTEREST

683 The authors declare no 695
684 competing financial interest.
685 696
686 697
687 698
688 699
689 700
690 701
691 702
692 703
693 704
694

705 LIST OF SYMBOLS

706 SEO polystyrene-b-poly(ethylene oxide)
707 PEO-POSS poly(ethylene oxide)-b-polyhedral oligomeric silsesquioxane
708 PEO poly(ethylene oxide)
709 POSS polyhedral oligomeric silsesquioxane
710 LiTFSI lithium bis(trifluoromethanesulfonyl)imide
711 r ratio of lithium to ethylene oxide moieties
712 -R alkyl substituent group on POSS silica cage
713 M_{POSS} molar mass of POSS (g/mol)
714 M_{PEO} molar mass of PEO (g/mol)
715 $f_{\text{EO/LiTFSI}}$ volume fraction of EO and LiTFSI phase
716 N degree of polymerization
717 SAXS small angle x-ray scattering
718 I scattering intensity
719 q scattering vector (nm^{-1})
720 I_{abs} absolute scattering intensity (cm^{-1})
721 κ ionic conductivity (S/cm)

| | | |
|-----|---------------------------|--|
| 722 | ρ_+ | current fraction |
| 723 | $R_{i,0}$ | initially measured interfacial resistance |
| 724 | $R_{i,0}$ | interfacial resistance measured at steady-state |
| 725 | ΔV | applied potential |
| 726 | i_0 | measure of the initial current, as defined as the ratio of applied |
| 727 | | potential to sum of bulk and interfacial resistances |
| 728 | $t_{+,ss}$ | steady-state cationic transference number |
| 729 | D | salt diffusion coefficient (cm^2/s) |
| 730 | q^* , $2q^*$, $3q^*$ | scattering peaks |
| 731 | FWHM | full-width-half-max |
| 732 | TEM | transmission electron microscopy |
| 733 | d | domain spacing |
| 734 | LAM | lamellar |
| 735 | DIS | disordered |
| 736 | COEX/LAM | coexistence of ordered lamellar phases |
| 737 | ϕ_c | volume fraction of conducting phase |
| 738 | κ_n | normalized conductivity |
| 739 | κ_{PEOPOSS} | conductivity of PEO-POSS (S/cm) |
| 740 | κ_{PEO} | conductivity of PEO (S/cm) |
| 741 | ω | angular frequency |
| 742 | G' | storage modulus |
| 743 | G'' | loss modulus |

744

745 REFERENCES AND NOTES

- 746(1) Fenton, D. E.; Parker, J. M.; Wright, P. V. Complexes of Alkali Metal Ions
747 with Poly(Ethylene Oxide). *Polymer*. **1973**, *14* (11), 589.
- 748(2) Tarascon, J. M.; Armand, M. Issues and Challenges Facing
749 Rechargeable Lithium Batteries. *Nature* **2001**, *414* (6861), 359–367.

- 750(3) Goodenough, J. B.; Kim, Y. Challenges for Rechargeable Li Batteries.
751 *Chem. Mater.* **2010**, 22 (3), 587-603.
- 752(4) Armand, M. Polymer Solid Electrolytes - an Overview. *Solid State Ionics*
753 **1983**, 9-10, 745-754.
- 754(5) Balsara, N. P.; Newman, J. Comparing the Energy Content of Batteries,
755 Fuels, and Materials. *J. Chem. Educ.* **2013**, 90 (4), 446-452.
- 756(6) Monroe, C.; Newman, J. The Impact of Elastic Deformation on
757 Deposition Kinetics at Lithium/Polymer Interfaces. *J. Electrochem. Soc.*
758 **2005**, 152 (2), A396.
- 759(7) Singh, M.; Odusanya, O.; Park, M. J.; Iatrou, H.; Wilmes, G. M.; Eitouni,
760 H. B.; Fragouli, P.; Patel, A. J.; Hadjichristidis, N.; Balsara, N. P.; Effect of
761 Molecular Weight on the Mechanical and Electrical Properties of Block
762 Copolymer Electrolytes. *Macromolecules* **2007**, 40 (13), 4578-4585.
- 763(8) Villaluenga, I.; Chen, X. C.; Devaux, D.; Hallinan, D. T.; Balsara, N. P.
764 Nanoparticle-Driven Assembly of Highly Conducting Hybrid Block
765 Copolymer Electrolytes. *Macromolecules* **2015**, 48 (2), 358-364.
- 766(9) Soo, P. P.; Huang, B.; Jang, Y.-I.; Chiang, Y.-M.; Sadoway, D. R.; Mayes,
767 A. M. Rubbery Block Copolymer Electrolytes for Solid-State
768 Rechargeable Lithium Batteries. *J. Electrochem. Soc.* **1999**, 146 (1),
769 32.
- 770(10) Ruzette, A.-V. G.; Soo, P. P.; Sadoway, D. R.; Mayes, A. M. Melt-
771 Formable Block Copolymer Electrolytes for Lithium Rechargeable
772 Batteries. *J. Electrochem. Soc.* **2002**, 148 (6), A537.

- 773(11) Kosonen, H.; Valkama, S.; Hartikainen, J.; Eerikäinen, H.; Torkkeli, M.;
774 Jokela, K.; Serimaa, R.; Sundholm, F.; Ten Brinke, G.; Ikkala, O.
775 Mesomorphic Structure of Poly(Styrene)-Block-Poly(4-Vinylpyridine)
776 with Oligo(Ethylene Oxide)Sulfonic Acid Side Chains as a Model for
777 Molecularly Reinforced Polymer Electrolyte. *Macromolecules* **2002**, *35*
778 (27), 10149–10154.
- 779(12) Trapa, P. E.; Huang, B.; Won, Y.-Y.; Sadoway, D. R.; Mayes, A. M. Block
780 Copolymer Electrolytes Synthesized by Atom Transfer Radical
781 Polymerization for Solid-State, Thin-Film Lithium Batteries.
782 *Electrochem. Solid-State Lett.* **2002**, *5* (5), A85.
- 783(13) Epps, T. H.; Bailey, T. S.; Waletzko, R.; Bates, F. S. Phase Behavior and
784 Block Sequence Effects in Lithium Perchlorate-Doped Poly(Isoprene-b-
785 Styrene-b-Ethylene Oxide) and Poly(Styrene-b-Isoprene-b-Ethylene
786 Oxide) Triblock Copolymers. *Macromolecules* **2003**, *36* (8), 2873–2881.
- 787(14) Cho, B.-K.; Jain, A.; Gruner, S. M.; Wiesner, U. Mesophase Structure-
788 Mechanical and Ionic Transport Correlations in Extended Amphiphilic
789 Dendrons. **2004**, *305*, 1598–1602.
- 790(15) Panday, A.; Mullin, S.; Gomez, E. D.; Wanakule, N.; Chen, V. L.;
791 Hexemer, A.; Pople, J.; Balsara, N. P. Effect of Molecular Weight and
792 Salt Concentration on Conductivity of Block Copolymer Electrolytes.
793 *Macromolecules* **2009**, *42* (13), 4632–4637.

- 794(16) Young, W. S.; Epps, T. H. Salt Doping in PEO-Containing Block
795 Copolymers: Counterion and Concentration Effects. *Macromolecules*
796 **2009**, 42 (7), 2672–2678.
- 797(17) Mullin, S. A.; Stone, G. M.; Panday, A.; Balsara, N. P. Salt Diffusion
798 Coefficients in Block Copolymer Electrolytes. *J. Electrochem. Soc.*
799 **2011**, 158 (6), A619.
- 800(18) Gunkel, I.; Thurn-Albrecht, T. Thermodynamic and Structural Changes
801 in Ion-Containing Symmetric Diblock Copolymers: A Small-Angle X-Ray
802 Scattering Study. *Macromolecules* **2012**, 45 (1), 283–291.
- 803(19) Young, W. S.; Epps, T. H. Ionic Conductivities of Block Copolymer
804 Electrolytes with Various Conducting Pathways: Sample Preparation
805 and Processing Considerations. *Macromolecules* **2012**, 45 (11), 4689–
806 4697.
- 807(20) Teran, A. A.; Balsara, N. P. Thermodynamics of Block Copolymers with
808 and without Salt. *J. Phys. Chem. B* **2014**, 118 (1), 4–17.
- 809(21) Irwin, M. T.; Hickey, R. J.; Xie, S.; So, S.; Bates, F. S.; Lodge, T. P.
810 Structure-Conductivity Relationships in Ordered and Disordered Salt-
811 Doped Diblock Copolymer/Homopolymer Blends. *Macromolecules*
812 **2016**, 49 (18), 6928–6939.
- 813(22) Loo, W. S.; Jiang, X.; Maslyn, J. A.; Oh, H. J.; Zhu, C.; Downing, K. H.;
814 Balsara, N. P. Reentrant Phase Behavior and Coexistence in
815 Asymmetric Block Copolymer Electrolytes. *Soft Matter* **2018**, 14 (15),
816 2789–2795.

817

818

819

820(23) Sethi, G. K.; Jiang, X.; Chakraborty, R.; Loo, W. S.; Villaluenga, I.;
821 Balsara, N. P. Anomalous Self-Assembly and Ion Transport in
822 Nanostructured Organic-Inorganic Solid Electrolytes. *ACS Macro Lett.*
823 **2018**, 7 (9), 1056–1061.

824(24) Ratner, M. A.; Johansson, P.; Shriver, D. F. Polymer Electrolytes: Ionic
825 Transport Mechanisms and Relaxation Coupling. *MRS Bull.* **2000**, 25,
826 31.

827(25) Li, G.; Charles, U. P. Polyhedral Oligomeric Silsesquioxane (POSS)
828 Polymers, Copolymers, and Resin Nanocomposites. *Macromol. Contain.*
829 *Met. Met. Elem. Gr. IVA Polym.* **2005**, 4 (3), 79–131.

830(26) Matějka, L.; Strachota, A.; Pleštil, J.; Whelan, P.; Steinhart, M.; Šlouf, M.
831 Epoxy Networks Reinforced with Polyhedral Oligomeric Silsesquioxanes
832 (POSS). Structure and Morphology. *Macromolecules* **2004**, 37 (25),
833 9449–9456.

834(27) Ni, Y.; Zheng, S.; Nie, K. Morphology and Thermal Properties of
835 Inorganic-Organic Hybrids Involving Epoxy Resin and Polyhedral
836 Oligomeric Silsesquioxanes. *Polymer (Guildf).* **2004**, 45 (16), 5557–
837 5568.

- 838(28) Fina, A.; Tabuani, D.; Frache, A.; Camino, G. Polypropylene-Polyhedral
839 Oligomeric Silsesquioxanes (POSS) Nanocomposites. *Polymer*. **2005**,
840 46, 7855–7866.
- 841(29) Pracella, M.; Chionna, D.; Fina, A.; Tabuani, D.; Frache, A.; Camino, G.
842 Polypropylene-POSS Nanocomposites: Morphology and Crystallization
843 Behaviour. *Macromol. Symp.* **2006**, 234, 59–67.
- 844(30) Perrin, F. X.; Panaitescu, D. M.; Frone, A. N.; Radovici, C.; Nicolae, C.
845 The Influence of Alkyl Substituents of POSS in Polyethylene
846 Nanocomposites. *Polymer*. **2013**, 54 (9), 2347–2354.
- 847(31) Heeley, E. L.; Hughes, D. J.; El Aziz, Y.; Williamson, I.; Taylor, P. G.;
848 Bassindale, A. R. Properties and Self-Assembled Packing Morphology of
849 Long Alkyl-Chained Substituted Polyhedral Oligomeric Silsesquioxanes
850 (POSS) Cages. *Phys. Chem. Chem. Phys.* **2013**, 15 (15), 5518–5529.
- 851(32) Lu, Y. S.; Kuo, S. W. Functional Groups on POSS Nanoparticles Influence
852 the Self-Assembled Structures of Diblock Copolymer Composites. *RSC*
853 *Adv.* **2014**, 4 (66), 34849–34859.
- 854(33) Heeley, E. L.; Hughes, D. J.; El Aziz, Y.; Taylor, P. G.; Bassindale, A. R.
855 Morphology and Crystallization Kinetics of Polyethylene/Long Alkyl-
856 Chain Substituted Polyhedral Oligomeric Silsesquioxanes (POSS)
857 Nanocomposite Blends: A SAXS/WAXS Study. *Eur. Polym. J.* **2014**, 51
858 (1), 45–56.
- 859(34) Niemczyk, A.; Dziubek, K.; Sacher-Majewska, B.; Czaja, K.; Dutkiewicz,
860 M.; Marciniak, B. Study of Thermal Properties of Polyethylene and

- 861 Polypropylene Nanocomposites with Long Alkyl Chain-Substituted POSS
862 Fillers. *J. Therm. Anal. Calorim.* **2016**, *125* (3), 1287-1299.
- 863(35) Ueda, K.; Tanaka, K.; Chujo, Y. Synthesis of POSS Derivatives Having
864 Dual Types of Alkyl Substituents and Their Application as a Molecular
865 Filler for Low-Refractive and Highly Durable Materials. *Bull. Chem. Soc.*
866 *Jpn.* **2017**, *90* (2), 205-209.
- 867(36) Miao, J.; Cui, L.; Lau, H. P.; Mather, P. T.; Zhu, L. Self-Assembly and
868 Chain-Folding in Hybrid Coil-Coil-Cube Triblock Oligomers of
869 Polyethylene-b-Poly(Ethylene Oxide)-b-Polyhedral Oligomeric
870 Silsesquioxane. *Macromolecules* **2007**, *40* (15), 5460-5470.
- 871(37) Yu, X.; Zhong, S.; Li, X; Tu, Y.; Yang, S.; Van Horn, R.; Ni, C.; Pochan, D.
872 J.; Quirk, R. P.; Wesdemiotis, C.; Zhang, W.; Cheng, S. Z. D. A Giant
873 Surfactant of Polystyrene- (Carboxylic Acid-Functionalized Polyhedral
874 Oligomeric Silsesquioxane) Amphiphile with Highly Stretched
875 Polystyrene Tails in Micellar Assemblies. *J. Am. Chem. Soc.* **2010**, *132*
876 (47), 16741-16744.
- 877(38) Huang, M.; Hsu, C.; Wang, J.; Mei, S.; Dong, X.; Li, Y.; Li, M.; Liu, H.;
878 Zhang, W.; Aida, T.; Zhang, W.; Yue, K.; Cheng, S. Z. D. Selective
879 Assemblies of Giant Tetrahedra via Precisely Controlled Positional
880 Interactions. *Science*. **2015**, *348* (6233), 424-428.
- 881(39) Sax, J.; Ottino, J. M. Modeling of transport of small molecules in polymer
882blends:

883 Application of effective medium theory. *Polymer Engineering and*
884 *Science*. **1983**, 23 (3), 165-176.

885(40) Kambe, Y.; Arge, C. G.; Patel, S. N.; Stoykovich, M. P.; Nealey, P. F. Ion
886Conduction in
887 Microphase-Separated Block Copolymer Electrolytes. *Electrochem. Soc.*
888*Interface* **2017**,
889 26, 61-67.

890(41) Hexemer, A.; Bras, W.; Glossinger, J.; Schaible, E.; Gann, E.; Kirian, R.;
891 MacDowell, A.; Church, M.; Rude, B.; Padmore, H. A
892 SAXS/WAXS/GISAXS Beamline with Multilayer Monochromator. *J. Phys.*
893 *Conf. Ser.* **2010**, 247.

894(42) Ilavsky, J. Nika: Software for Two-Dimensional Data Reduction. *J. Appl.*
895 *Crystallogr.* **2012**, 45 (2), 324-328.

896(43) Newman, J.; Chapman, T. W. Restricted Diffusion in Binary Solutions.
897 *AIChE J.* **1973**, 19 (2), 343-348.

898(44) Bruce, P. G.; Hardgrave, M. T.; Vincent, C. A. Steady State Current Flow
899 in Solid Binary Electrolyte Cells. *J. Electroanal. Chem. Interfacial*
900 *Electrochem.* **2002**, 271 (1-2), 27-34.

901(45) Galluzzo, M. D.; Maslyn, J. A.; Shah, D. B.; Balsara, N. P. Ohm's law for
902 ion conduction in lithium and beyond-lithium battery electrolytes. *The*
903 *Journal of Chemical Physics.* **2019**, 151.

904(46) Balsara, N. P.; Newman, J. Relationship between Steady-State Current
905 in Symmetric Cells and Transference Number of Electrolytes

906 Comprising Univalent and Multivalent Ions. *J. Electrochem. Soc.* **2015**,
907 162 (14), A2720 – A2722.

908(47) Villaluenga, I.; Pesko, D. M.; Timachova, K.; Feng, Z.; Newman, J.;
909 Srinivasan, V.; Balsara, N. P. Negative Stefan-Maxwell Diffusion
910 Coefficients and Complete Electrochemical Transport Characterization
911 of Homopolymer and Block Copolymer Electrolytes. *J. Electrochem.*
912 *Soc.* **2015**, 162 (3), A398–A405.

913(48) Schauer, N. S.; Harry, K. J.; Parkinson, D. Y.; Watanabe, H.; Balsara, N.
914 P. Lithium Dendrite Growth in Glassy and Rubbery Nanostructured
915 Block Copolymer Electrolytes. *J. Electrochem. Soc.* **2018**, 165 (11),
916 A2766–A2773

917(49) Leibler, L. Theory of Microphase Separation in Block Copolymers.
918 *Macromolecules* **1980**, 13 (6), 1602–1617.

919(50) Thelen, J. L.; Teran, A. A.; Wang, X.; Garetz, B. A.; Nakamura, I.; Wang,
920 Z. G.; Balsara, N. P. Phase Behavior of a Block Copolymer/Salt Mixture
921 through the Order-to-Disorder Transition. *Macromolecules* **2014**, 47
922 (8), 2666–2673.

923(51) Shim, J.; Bates, F. S.; Lodge, T. P. Superlattice by charged block
924 copolymer self-assembly. *Nature Communications*. **2019**, 10, 2108.

925(52) Teran, A. A.; Tang, M. H.; Mullin, S. A.; Balsara, N. P. Effect of molecular
926 weight on conductivity of polymer electrolytes. *Solid State Ionics*.
927 **2011**, 203, 18–21.

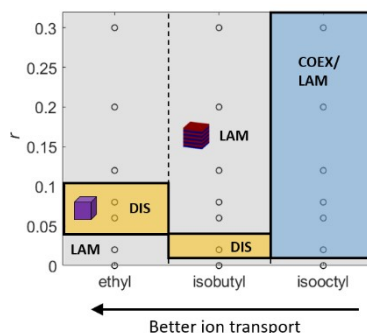
928

929 **GRAPHICAL ABSTRACT**

930 Kevin W. Gao, Xi Jiang, Zach J. Hoffman, Gurmukh K. Sethi, Saheli
931 Chakraborty, Irune Villaluenga, Nitash P. Balsara

932 Optimizing the Monomer Structure of Polyhedral Oligomeric Silsesquioxane
933 (POSS) for Ion Transport in Hybrid Organic-Inorganic Block Copolymers

934 Poly(ethylene oxide)-*b*-polyhedral oligomeric silsesquioxane (PEO-POSS)
935 mixed with lithium salt is a nanostructured hybrid organic-inorganic block
936 copolymer electrolyte that may enable lithium metal batteries. Three PEO-
937 POSS electrolytes which only differ by their POSS substituents (ethyl,
938 isobutyl, isoctyl) are synthesized and characterized. Salt-induced mixing of
939 the two blocks becomes less effective as the length of the POSS alkyl chain
940 substituent is increased. The ethyl substituent is shown to be optimal for ion



941 transport.

942